Enhanced electrochemical properties of ball-milled γ'-V2O5 as cathode material for Na-ion batteries: A structural and kinetic investigation

Rita Baddour-Hadjean, Marianne Safrany Renard, J.-P. Pereira-Ramos

Enhanced Electrochemical Properties of Ball-Milled γ'-V_2O_5 as Cathode Material for Na-ion Batteries: A Structural and Kinetic Investigation

Rita Baddour-Hadjean*, Marianne Safrany Renard, Jean-Pierre Pereira-Ramos[+]

Institut de Chimie et des Matériaux Paris Est (ICMPE), UMR 7182 CNRS-Université Paris Est Créteil, 2 rue Henri Dunant, 94320 Thiais, France

*corresponding author: baddour@icmpe.cnrs.fr, ORCID ID 0000-0002-3158-1851
[+]ORCID ID 0000-0001-5381-900X

Abstract: The recent intensive research for cathode materials beyond Li-ion batteries has revitalized interest in V_2O_5 due to its high reversible capacity. Among the various polymorphs, γ'-V_2O_5 exhibits a unique corrugated layered structure that promotes the insertion of guest species. However, when used as cathode material for SIB, this material suffers from a 50% first charge efficiency that prevents the full benefit of its high discharge capacity of 140 mAh g^{-1}. Herein, we demonstrate and explain the effectiveness of a ball-milling approach to overcome this strong limitation. Several positive impacts of particle size reduction are highlighted: the charge efficiency is increased to 90%, allowing a 2-fold enhancement of the available capacity upon cycling (120 mAh g^{-1} after 50 cycles at C/2). The Na insertion mechanism investigated by XRD and Raman spectroscopy shows a peculiar behavior with wide solid solution domains at the expense of the diphasic region. The kinetics study reveals a faster diffusivity in the ball-milled material and enhanced Na diffusion in the single-phase region. Both structural and kinetic reversibility account for the high performance here achieved for γ'-V_2O_5: a high working voltage of 3.2 V vs Na^+/Na, a high rate capability, excellent charge efficiency and good cycle life.

Keywords: γ'-V_2O_5, Na-ion battery, cathode material, ball-milling, electrochemical properties, kinetics

1. Introduction

In the past several years, sodium-ion batteries (SIBs) have received considerable interest as possible alternative to lithium-ion batteries (LIBs) because of the high cost and low availability of Li sources, especially in the context of large-scale batteries. The main challenge for SIBs is to develop high performance cathode and anode materials. As the fundamental principle of SIBs is identical to that of LIBs, many of the electrode materials used for LIBs have been mimicked in designing several SIBs electrode materials [1, 2]. In particular, among the cathode systems, various sodiated oxides have been explored such as Na_xCoO_2 [3], $Na_{2/3}(Fe_{0.5}Mn_{0.5})O_2$ [4], $NaMnO_2$ [5], $NaCrO_2$ [6], Na_xVO_2 [7, 8], $Na_{1+y}V_3O_8$ [9], $Na_{0.33}V_2O_5$ [10, 11].

Orthorhombic-layered α-V_2O_5 was early proposed as host material for Na^+ storage [12]. Recently, this compound regained interest as cathode material for SIBs due to its high theoretical capacity as well as significant progress achieved towards its application in LIBs. Our group investigated the Na^+ storage mechanism of α-V_2O_5 through *ex situ* X-ray diffraction (XRD) and Raman spectroscopy [13]. It was found that Na insertion is more difficult than Li one : the initial phase transformation from α-V_2O_5 to α-NaV_2O_5 phase occurs at low voltage of 1.8 V vs Na^+/Na and is irreversible after subsequently charging back to 4.0 V. However, the accommodation of 0.8 additional mobile Na ions can be achieved in the electroformed NaV_2O_5 bronze, allowing a rechargeable capacity of 80-100 mAh g^{-1} to be reached with good retention upon cycling [13]. The presence of pillaring interlayer Na^+ ions was suggested to be responsible for the high retaining of the NaV_2O_5 host structure on guest cation insertion [13, 14].

On the other hand, our recent studies have demonstrated the interest of the puckered γ'-V_2O_5 polymorph (also belonging to an orthorhombic system but with a larger interlayer spacing than α-V_2O_5). Superior electrochemical performance toward Li^+ [15, 16] and Na^+ [17-20] insertion were revealed compared to α-V_2O_5 [13, 18], the corrugated structure of γ'-V_2O_5 being able to

accommodate almost 1 Na^+/mol., remarkably at the same working voltage than Li^+, which leads to a specific capacity of 145 mAh g^{-1} available at 3.3V vs Na^+/Na. However, this cathode material was shown to suffer from a poor charge efficiency in the first cycle that does not exceed 50% at moderate rate. A structural investigation through XRD and Raman spectroscopy has allowed to establish the Na^+ storage mechanism of γ'-V_2O_5 for $0 \leq x \leq 1$ in γ-$Na_xV_2O_5$ [17] while a kinetic investigation outlined the strong dependence of Na diffusivity and other fundamental parameters with the sodium content [19]. A large expansion in unit cell volume (+17%) was highlighted during the sodiation, probably responsible for a loss of inter-particles contact impeding the desodiation process. In a first attempt to improve the first charge efficiency, a preliminary downsizing approach was carried out on the as-synthesized γ'-V_2O_5 powder using planetary ball-milling [18]. As a result, the charge capacity was found to reach more than 100 mAh g^{-1} at 1C for the ball-milled material against only 40 mAh g^{-1} for the pristine one. Such enhancement suggests a faster kinetics in the ball-milled powder, even if a nanosize effect on the structural response of the γ'-V_2O_5 host lattice cannot be ruled out.

In the present work, we investigate in details the impact of the particle size reduction afforded by a ball-milling approach on the electrochemical properties of γ'-V_2O_5 as cathode material for Na-ion batteries. The origin of the performance enhancement observed on the ball-milled material is examined at the light of a structural study based upon XRD and Raman experiments. In addition, the kinetic parameters of the electrochemical Na insertion-extraction reaction in ball-milled γ'-V_2O_5 are investigated as a function of x in γ-$Na_xV_2O_5$ ($0 \leq x < 1$), using electrochemical impedance spectroscopy (EIS). The achieved findings allow getting a full understanding of the improved electrochemical properties of this promising cathode for SIBs.

2. Experimental

γ'-V_2O_5 was obtained by chemical oxidation of γ-LiV_2O_5 synthesized using the carbothermal reduction method [21]. Deinsertion of Li from the γ-LiV_2O_5 bronze was performed by reacting 500 mg of the bronze in a solution of NO_2BF_4 (solid Alfa Aesar 96%,) in acetonitrile (V_2O_5/NO_2BF_4 molar ratio 1/4) under stirring for 24h at room temperature. These experimental conditions ensure the quantitative Li extraction from the γ-LiV_2O_5 precursor. After reaction and decantation, the supernatant liquid is removed by pipetting. Powder is washed three times with acetonitrile, and then vacuum dried at 70°C for 24h. The powder color changes from black to orange, which confirms the complete lithium deintercalation. Electrochemical titration using galvanostatic oxidation and chemical redox titration confirmed the 5+ oxidation state of vanadium in γ'-V_2O_5. In addition, the powder color changes from black to orange, indicating the loss of the metallic properties for the fully deintercalated γ'-phase.

Size reduction of the as-synthesized γ'-V_2O_5 powder was performed in a planetary ball mill (Fritsch Pulverisette P7). γ'-V_2O_5 (1g at one time) was placed in the milling jar along with stainless steel balls (1 g and 7 mm diameter each) before the jar was sealed tightly. The ball to powder weight ratio was 39:1. The ball-milling protocol consisted in 10 mn milling times sequences (3, 4 and 6 milling times sequences) separated by 10 mn resting in order to avoid the overheating of the material. The resulting powders (called BM-30 γ'-V_2O_5, BM-40 γ'-V_2O_5 and BM-60 γ'-V_2O_5, respectively) were characterized by scanning electron microscopy (SEM), using a Zeiss Merlin-type microscope.
Electrochemical experiments were conducted at 20°C in two-electrode coin cells (CR2032) with sodium disk as reference and negative electrodes. The separator consisted of three glass Whatman microfiber filters as soaked by a solution 1 M $NaClO_4$ in propylene carbonate (PC) containing fluoroethylene carbonate (FEC) additive (2% Vol.). The positive electrode is prepared by mixing 80 wt % of active material with 7.5 wt % of acetylene black, 7.5 wt % of graphite and 5 wt % of PTFE

as binder agent. About 8mg of this mixture was pressed on a stainless steel grid current collector (8 mm diam, 0.35 mm thick) under a pressure of 5 tons per cm^2. All the CR2032 coin-cells were assembled in an argon-filled glovebox where water and oxygen concentrations were kept less than 1 ppm. Impedance measurements were carried out at 20°C, using a conventional three electrode cells under argon atmosphere. The cell was filled with 1M $NaClO_4$ in PC. The positive electrode was made of the same composite electrode as the one used in coin cells. A Li wire placed in a separate compartment filled up with lithiated PC electrolyte ensured a reliable and stable reference potential while a high surface gold wire acted as counter electrode. The working electrode composition was adjusted by coulometric titration using a low current density (C/20 rate, 147 mA g^{-1} corresponding to 1C). Equilibrium was considered as reached when the open circuit voltage remained stable (<0.2 mV for 1h). The geometric surface area of the working electrode dipped in the 3-electrode cell for impedance measurements is 1 cm^2.

Impedance measurements were conducted in the 10^5 - 2 10^{-3} Hz frequency range. The excitation signal was 10 mV peak to peak. Galvanostatic and impedance experiments were performed using a VMP3 Biologic Multipotentiostat-Galvanostat apparatus.

The structural study was carried out on electrochemically formed γ-$Na_xV_2O_5$ samples prepared at C/10 discharge/charge rate. After 2 h of equilibrium time, the cell was opened in the glovebox and the positive electrode was removed, rinsed with dimethyl carbonate (DMC) and placed in appropriate airtight sample holders to be further analyzed by X-ray diffraction and Raman spectroscopy. XRD measurements were performed out using a Panalytical X'pert pro diffractometer equipped with an X'celerator detector and a Co Kα radiation (wavelength λ = 1.7889 Å). All the diffraction patterns were collected with a 2θ step of 0.0167°. Data were then processed on Eva software to score reflections then CelRef was used to calculate the lattice parameters. The Raman spectra were measured with a LaBRAM HR 800 (Jobin-Yvon-Horiba) Raman micro-spectrometer including Edge

filters and equipped for signal detection with a back illuminated charge coupled device detector (Spex CCD) cooled by Peltier effect to 200 K. A He:Ne laser (632.8 nm) was used as the excitation source. The spectra were measured in back-scattering geometry. The resolution was about 0.5 cm^{-1}. A long distance 50X LWD objective was used to focus the laser light on sample surface to a spot size of 1 μm^2. To avoid local heating of the sample, the power of the laser beam was adjusted to 0.2–0.5 mW with a neutral filter. Raman spectra have been recorded on 10 different spots of each electrode. This led to similar spectra for the 10 investigated points, whatever the Na uptake.

3. Results and discussion

3.1. Structural characterization

SEM images of as-synthesized and ball-milled BM-30, BM-40 and BM-60 γ'-V_2O_5 powders are shown in **Fig. 1A**. The as-prepared sample (**Fig. 1Aa**) consists of aggregates a few micrometers long and 500 nm thick. The 30mn ball-milled sample (BM-30 γ′-V_2O_5, see **Fig. 1Ab**) exhibits smaller agglomerates, with particles that never exceed 500 nm in diameter, which shows the efficiency of the ball-milling process in reducing the particle size. However, for longer milling times of 40 and 60 mn (**Figs. 1Ac-d**), one can notice the appearance of chip-shaped particles on the surface of larger grains suggesting the presence of a secondary phase.

The XRD patterns of as-synthesized and ball-milled BM-30, BM-40 and BM-60 γ'-V_2O_5 powders are shown in **Fig. 1B**. The XRD pattern of the pristine γ'-V_2O_5 powder (**Fig. 1Ba**) exhibits the characteristics *hkl* reflections corresponding to an orthorhombic structure (P*nma* space group) with unit cell parameters a = 9.95 Å, b = 3.59 Å, c = 10.04 Å [17]. The structure of γ'-V_2O_5 (inset in **Fig. 1B**) retains the layered V_2O_5 framework although puckering of the layers is observed. It displays the typical features of all V_2O_5 polymorphs, *i.e.* V_2O_5 chains running in the b-direction and connected

within the layers via V-O "ladder-steps", the layers being stacked along the *c* direction and held together by weak interlayer interactions. The XRD pattern of the 30mn ball-milled powder (**Fig. 1Bb**) exhibits the whole *hkl* lines of the orthorhombic P*nma* structure, indicating the retention of the γ'-V_2O_5 structure upon 30 mn milling time in the conditions described above. Lattice parameters of a = 9.92 Å, b = 3.58 Å, c = 10.06 Å are found close to the values of the pristine γ-V_2O_5. The broadening of the diffraction peaks compared to the pristine oxide points to a decrease in the crystallite size (from 90 to 35 nm using the Scherrer equation [18]), which shows once again the efficiency of the ball-milling process in reducing the crystallite size. However, longer milling times of 40 and 60 mn lead to the gradual transformation of γ'-V_2O_5 into α-V_2O_5 (**Figs. 1Bc-d**) as well as an increasing amorphization process. The transition toward the more stable α- polymorph is undoubtedly induced by overheating under these longer milling times. The Raman spectra of as-synthesized and ball-milled BM-30, BM-40 and BM-60 γ'-V_2O_5 powders (**Fig. S1** in SI) confirms the occurrence at the atomic scale of the γ'-to-α phase transformation for milling times of 40 and 60 mn. As a consequence, the electrochemical, structural and kinetic investigations have been performed on the BM-30 γ'-V_2O_5 powder.

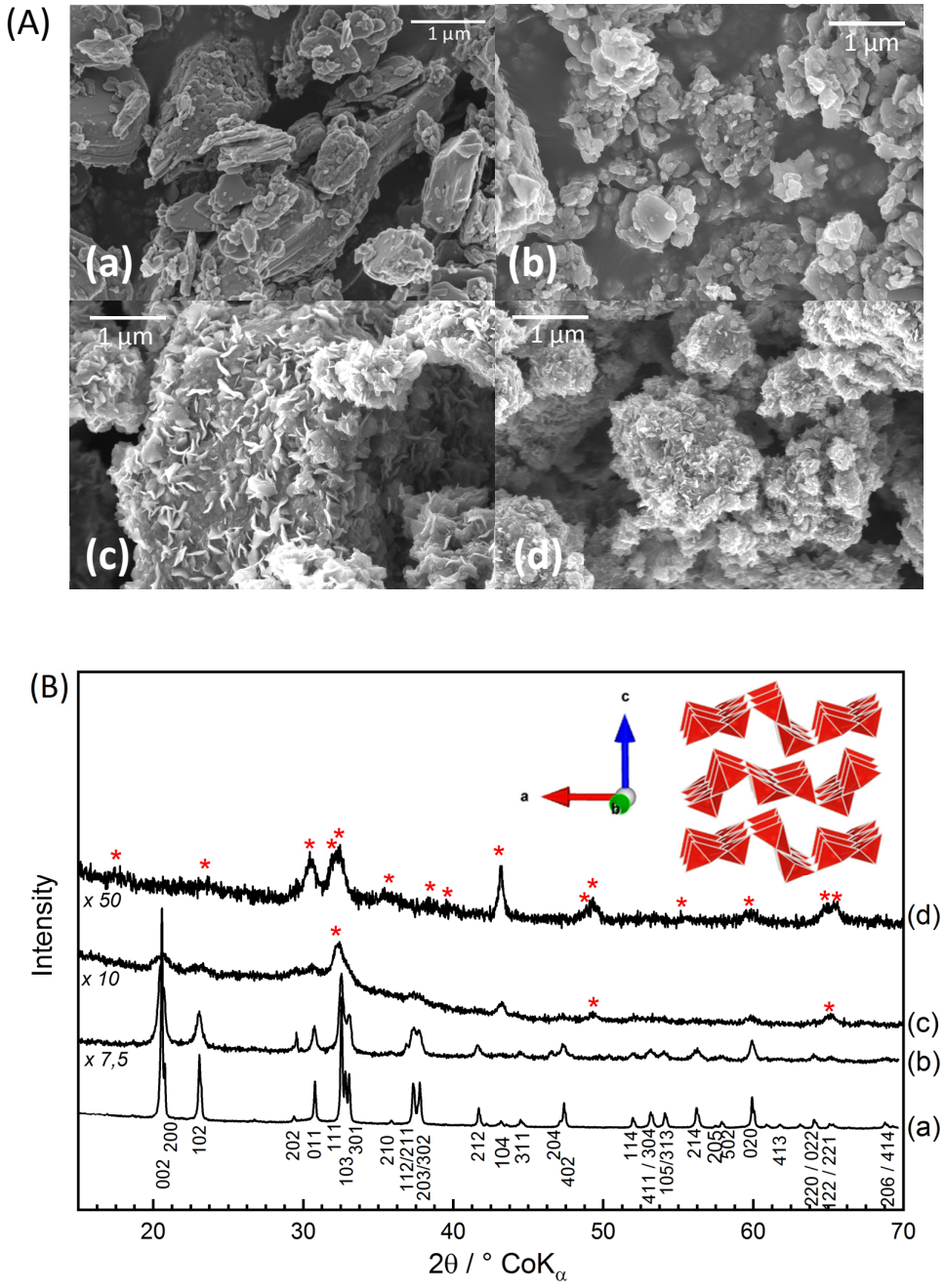

Figure 1. (A) SEM images and (B) XRD patterns of (a) as-synthesized (b) BM-30 (c) BM-40 (d) BM-60 γ'-V_2O_5. Red stars in Figure 1B: reflections of α-V_2O_5. Inset in Figure 1A: Crystalline structure of γ'-V_2O_5.

3.2. Electrochemical study

Fig. 2a and **Fig. S2** in SI show the strong impacts of the particle size reduction on the first discharge-charge curve of γ-V_2O_5. Firstly, a significant change in the discharge profile is observed: the well-defined discharge plateau near 3.2 V is greatly shortened for BM-30 γ-V_2O_5 to the benefit of a sloping curve involving the same specific capacity of 140 mAh g^{-1} (**Fig. 2a**). Second, the charge efficiency is significantly improved, from 52% at C/10 (75 mAh g^{-1}) for the pristine oxide to about 90% (i.e. 127 mAh g^{-1}) for BM-30 γ-V_2O_5. **Fig. S2** in SI shows the charge rate capability is even more improved for BM-30 γ-V_2O_5 for higher C rates, with for instance still 85 mAh g^{-1} available at 2C, i. e. three times higher than that recovered for the pristine oxide. As a consequence, further electrochemical cycles of BM-30 γ-V_2O_5 involve an enhanced discharge capacity of 120 mAh g^{-1} at C/2 (**Fig. 2b**), i.e. 50% larger than that observed for the as-synthesized sample at a lower C/5 rate (**Fig. 2c**). Furthermore, an excellent capacity retention is observed: a stable capacity of 120 mAh g^{-1} is achieved over 50 cycles at C/2 for the ball-milled material against only 70 and 55 mAh g^{-1} for the pristine oxide at C/10 and C/5 rate, respectively **(Fig. 2c)**.

The present observations also point to a particle size dependent voltage profile, as illustrated by **Fig. 2a** showing a wider sloping voltage domain for the ball-milled material. Such result is supported by open circuit voltage (OCV) measurements (see **Fig. 2d**) and indicates that another mechanism is at least contributing significantly to the curved voltage profile of BM-30 γ-V_2O_5. This finding prompted us to investigate the structural response of BM-30 γ-V_2O_5 upon sodiation and desodiation using XRD and Raman spectroscopy.

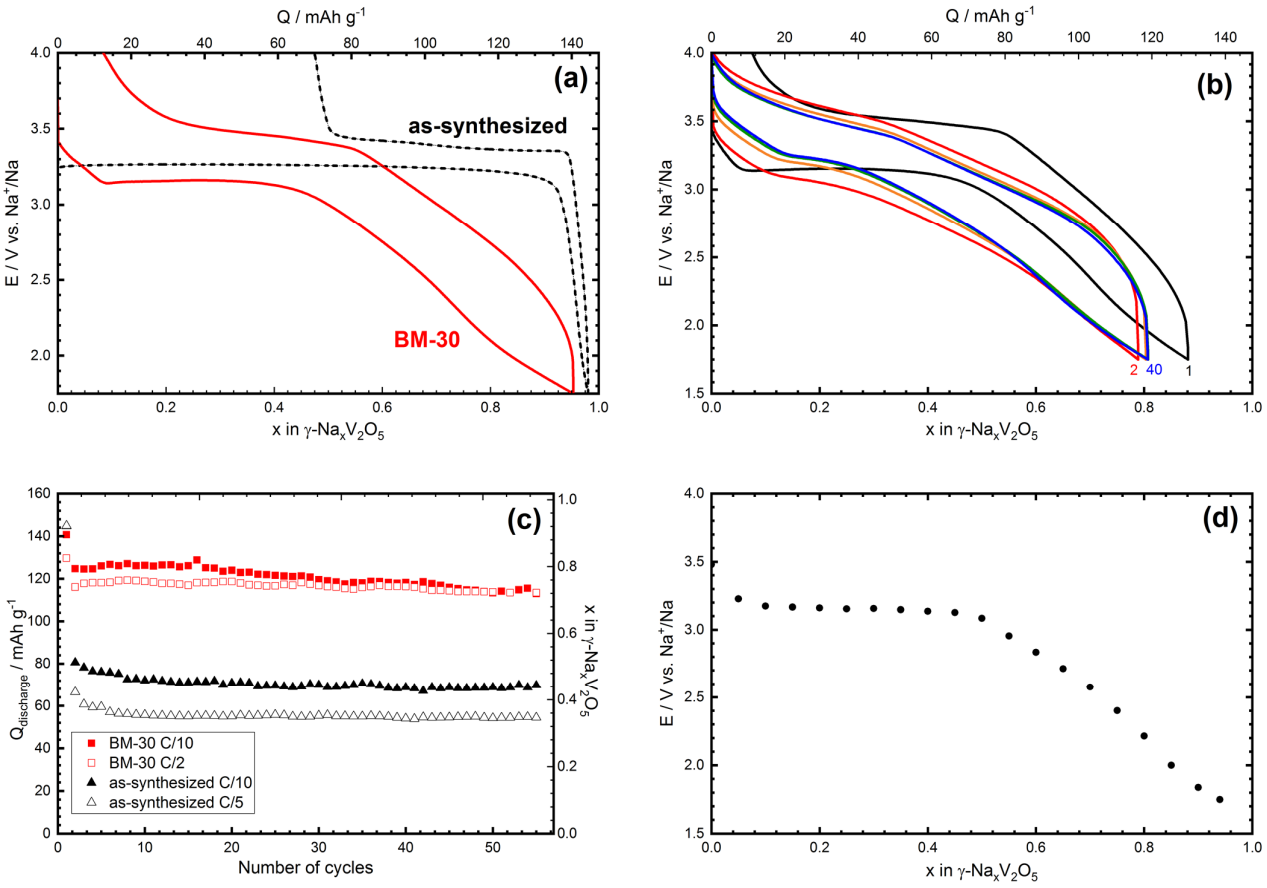

Figure 2. (a) First discharge-charge cycle at C/10 rate of as-synthesized and BM-30 γ'-V_2O_5 (b) Cycling curves of BM-30 γ'-V_2O_5 at C/2 rate (c) Evolution of the specific discharge capacity during cycling at different C-rates of as-synthesized γ'-V_2O_5 (black symbols △▲) and BM-30 γ'-V_2O_5 (red symbols □■) (d) OCV discharge curve of BM-30 γ'-V_2O_5 Electrolyte 1M $NaClO_4$ PC + FEC (2% vol.).

3.3. Structural mechanism during the first discharge-charge process

The XRD patterns of the BM-30 γ-$Na_xV_2O_5$ ($0 \leq x \leq 0.94$) electrodes recorded during the first discharge-charge process are reported in **Fig. 3**. As seen in **Fig. 3a**, during the very first part of the discharge (x = 0.05 and x =0.1), the typical orthorhombic fingerprint of the initial ball-milled material is kept. For x = 0.2, new reflections are observed (indicated by blue dashed lines), that coexist with those of the sodium-free material (indicated in red colour), indicating the presence of a diphasic domain. These new diffraction peaks can also be indexed in an orthorhombic cell (*Pnma* space group). However, as revealed by the position at lower 2θ value of the *002* line of the new

system (at 17.3° vs. 20.5°), the sodiated phase exhibits a larger *c* parameter (11.9 Å vs. 10.06 Å for the Na-free material). The two systems coexist in the narrow $0.2 \leq x < 0.4$ composition range, then a single-phase domain is observed for $0.4 \leq x \leq 0.94$, the XRD patterns being indexed according to a single orthorhombic sodiated γ-$Na_xV_2O_5$ phase. Upon charging, the XRD fingerprint of the pure sodiated phase is retained at least up to the mid-charge (**Fig. 3b**). For x = 0.3, some low intensity lines (*002*, *111*, *103*) belonging to γ'-V_2O_5 can be detected whereas the XRD pattern of the most oxidized sample (x = 0.1) is dominated by the *hkl* reflections of γ'-V_2O_5 (*002*, *102*, *111*, *103*) except the low intensity residual *002* peak corresponding to the sodiated phase. This indicates that a quasi-quantitative sodium extraction has taken place.

The detailed evolution of the lattice parameters as a function of sodium uptake x in discharged and charged BM-30 γ-$Na_xV_2O_5$ electrodes is shown in **Fig 4.** For $0 \leq x < 0.2$, a narrow single phase region is revealed accompanied by a negligible expansion of *a* parameter of 0.6 % while the *b* and *c* parameters are unchanged. This leads to a slight volume change, from 358 to 360 Å (+0.6 %) in that solid solution domain. In the narrow $0.2 \leq x < 0.4$ composition domain, where γ'-V_2O_5 and γ-$Na_xV_2O_5$ coexist, it is worth noting the large expansion of the *c* parameter for the early sodiated phase with composition γ-$Na_{0.2}V_2O_5$, characterized by a value of 11.89 Å, leading to a significant volume change of +18 % (**Fig. 4d**). Conversely, far more negligible variations are observed for the *a* and *b* parameters: *a* contracts by 1.2 % (9.98 to 9.86 Å) while *b* increases by only 0.1 % (**Figs. 4a-b**). Note the very slight changes in *a* and *b* parameters in γ-$Na_xV_2O_5$ within the $0.2 \leq x < 0.4$ solid solution range (- 0.8% for *a* and +0.6 % for *b*). The third composition region $0.4 \leq x \leq 0.94$ corresponds to a wide single-phase domain showing any detectable parameter change. Sodium ions are accommodated in the available interlayer sites of γ-$Na_{0.4}V_2O_5$ leading to the fully sodiated γ-$Na_{0.94}V_2O_5$ compound with the following unit cell parameters: *a* = 9.76 Å; *b* = 3.62 Å; *c* = 11.92 Å.

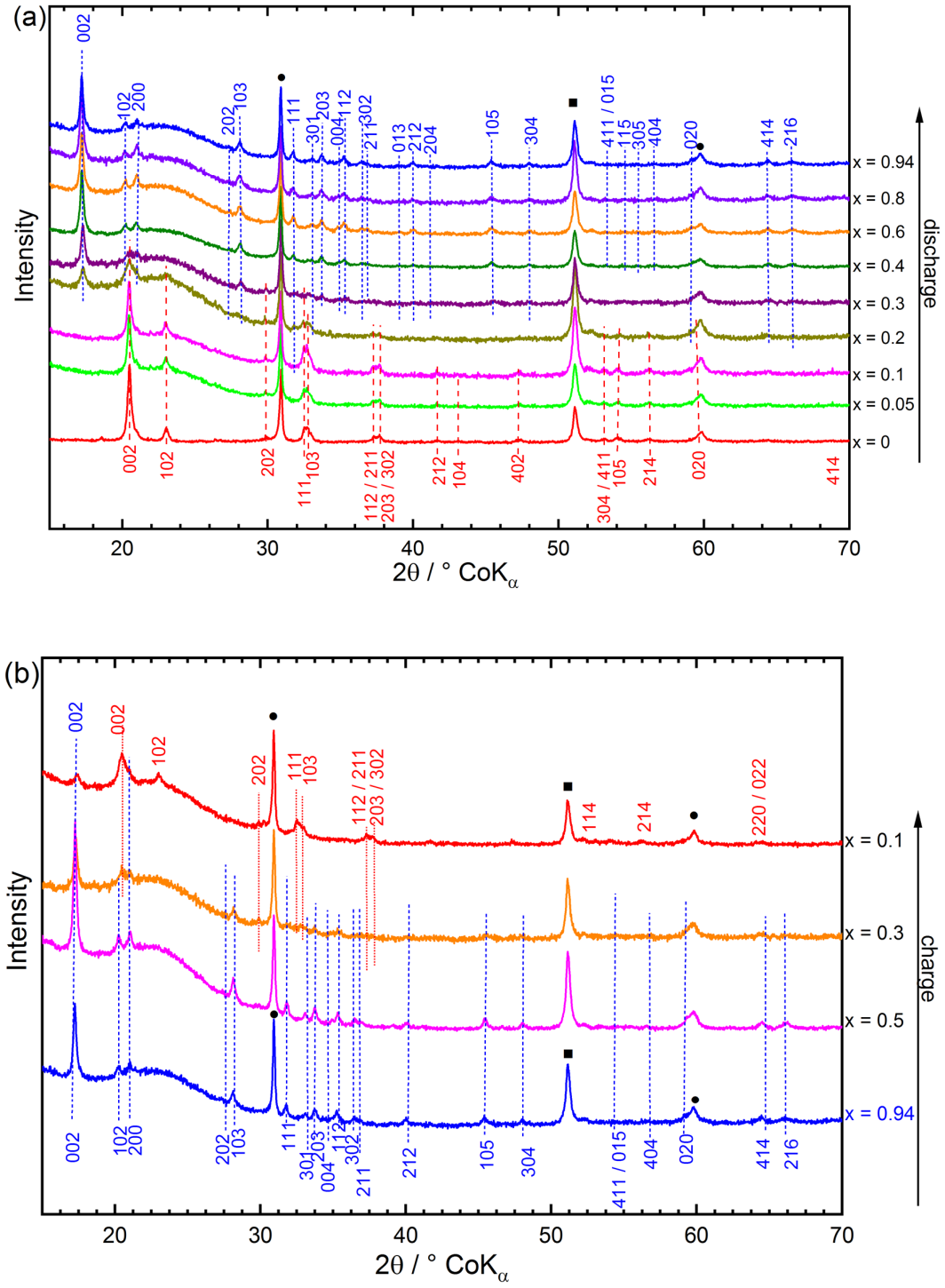

Figure 3. XRD patterns of BM-30 γ-$Na_xV_2O_5$ during the first discharge-charge cycle in 1M $NaClO_4$ PC + FEC (2% vol.) electrolyte; (a) discharge ($0 \leq x \leq 0.94$); (b) charge ($0.1 \leq x \leq 0.94$).
● Graphite peaks. ■ Stainless steel grid.

The evolution of the unit cell parameters and volumes during the charge (**Fig. 4**, ⊞ symbols) well superimpose to those found during the discharge. This demonstrates the high structural reversibility of the Na insertion reaction in BM-30 γ'-V_2O_5.

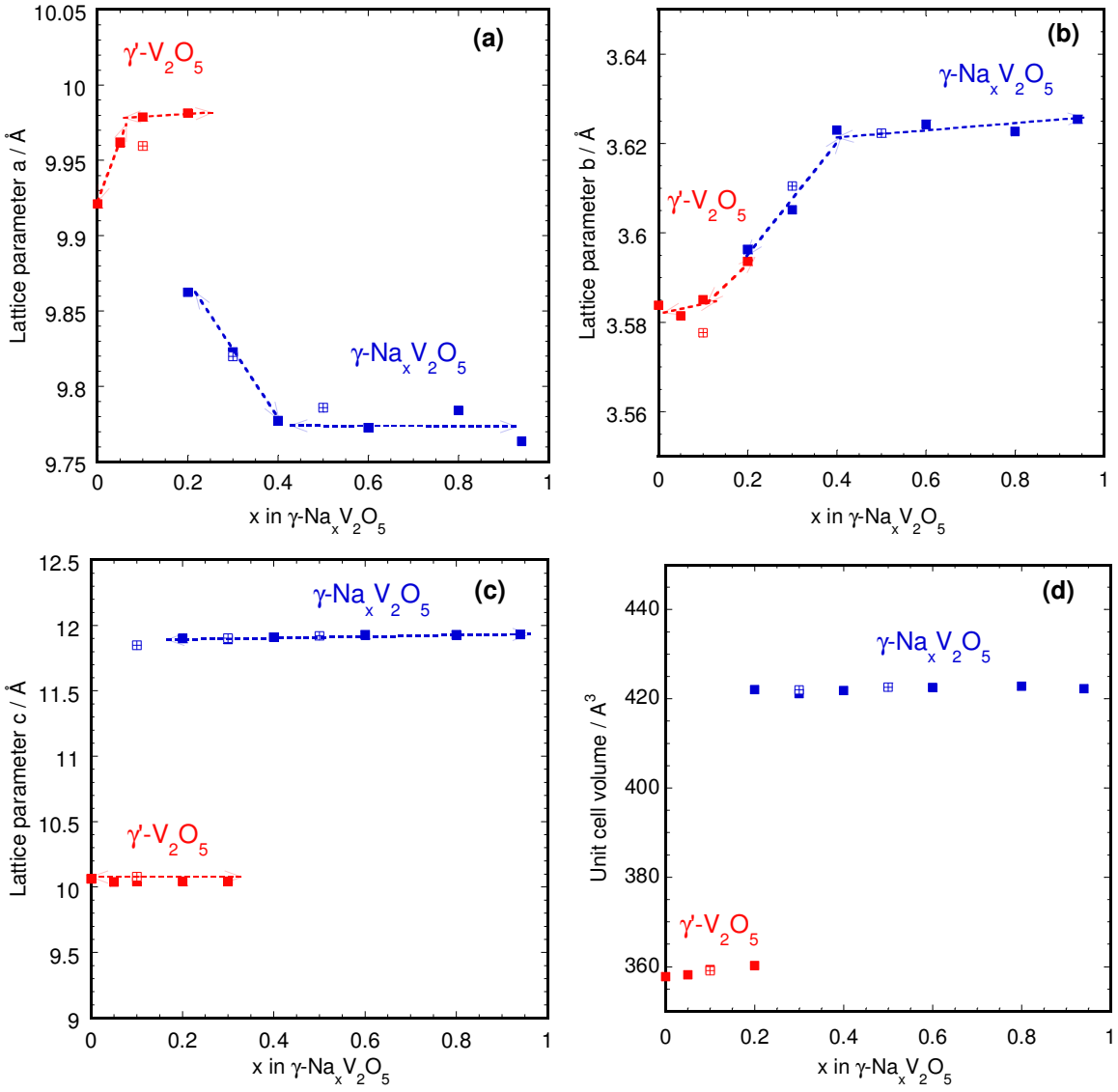

Figure 4. Evolution of (a-b-c) unit cell parameters and (d) volume of the phases formed during the first discharge-charge cycle of BM-30 γ'-V_2O_5 in 1M $NaClO_4$ PC + FEC (2% vol.) : ■ discharge ⊞ charge ($0 \leq x \leq 0.94$).

The Raman spectra of the BM-30 γ-$Na_xV_2O_5$ ($0 \leq x \leq 0.94$) electrodes recorded during the first discharge-charge process are gathered in **Fig. 5**. In good accord with the XRD findings, the emergence of the sodiated phase is observed from x = 0.2 with two new bands at 469 and 960 cm^{-1}

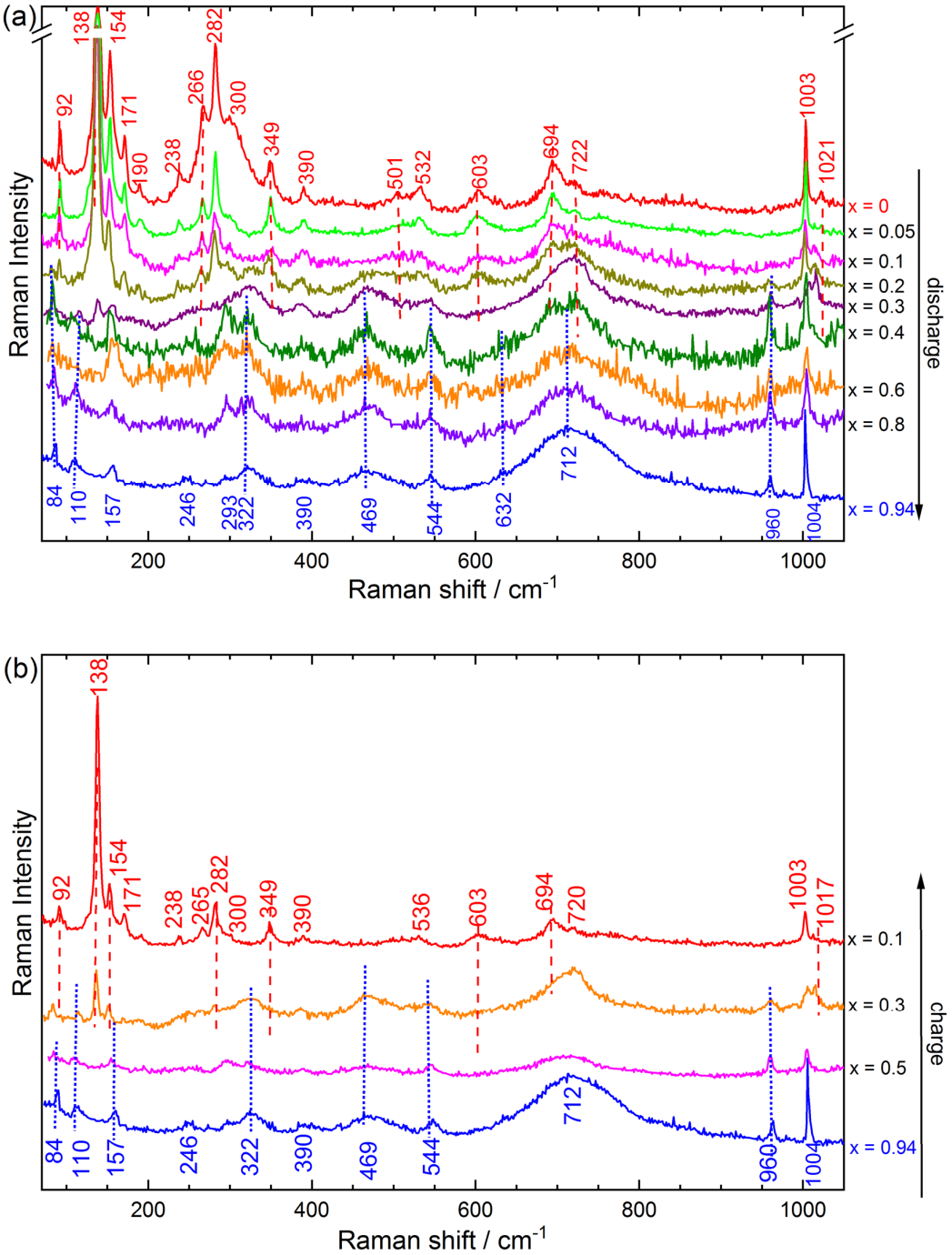

Figure 5. Raman spectra of BM-30 γ-$Na_xV_2O_5$ during the first discharge-charge cycle in 1M $NaClO_4$ PC + FEC (2% vol.) electrolyte: (a) discharge ($0 \leq x \leq 0.94$); (b) charge ($0.1 \leq x \leq 0.94$).

while the typical Raman fingerprint of the pristine oxide completely disappears for x = 0.4 (**Fig. 5a**). This is well illustrated by the absence of the low frequency band at 138 cm^{-1} and the high frequency vanadyl stretching vibration at 1021 cm^{-1} [22]. The pristine oxide and the sodiated phase coexist for x = 0.3, in agreement with the XRD study. The Raman spectra recorded during the charge (**Fig. 5b**) confirm the high structural reversibility of the Na insertion at the atomic scale, the pure Raman spectrum of γ'-V_2O_5 being recovered for x = 0.1 [22]. The residual sodiated phase detected by XRD in the most oxidized sample could not be observed, probably because the penetration depth of 100-500 nm is not sufficient enough to probe this small amount by Raman spectroscopy.

The present structural investigation provides a detailed picture of the Na insertion/extraction mechanism in the ball-milled BM-30 γ'-V_2O_5 material. The resulting phase diagram can be interestingly compared to that previously reported for the as-synthesized powder [17] in order to point to a particle size dependent mechanism, as suggested above from the voltage profile showing a wider sloping voltage domain for the ball-milled material (**Fig. 2a)**. The phase diagram of as-synthesized γ'-V_2O_5 consists in a very narrow solid solution with negligible structural changes for $x < 0.1$, followed by a wide diphasic region for $0.1 \leq x \leq 0.7$ and then a second solid solution domain for $0.7 < x \leq 0.97$ [17]. In the case of the present BM-30 γ'-V_2O_5, while the structural features for sodium-poor and sodium-rich phases are similar to the as-synthesized material, a strong enlargement of the solid solution domains is observed at the expense of the diphasic domain. Indeed, by reducing the particle size, the diphasic region is severely shrinked (from $0.1 \leq x \leq 0.7$ to $0.2 \leq x < 0.4$) while the single-phase domain is greatly extended (from $0.7 < x \leq 0.97$ to $0.4 \leq x \leq 0.94$). Such structural findings remarkably well explain the peculiar voltage profile showing a wider sloping voltage domain for the ball-milled γ'-V_2O_5 material (**Fig. 2a)**.

These results suggest that some discrepancy in the Na reaction kinetics should also be induced by the particle size reduction, as revealed by the huge first charge efficiency and rate capability improvement illustrated in **Fig. S2**. This prompted us to examine in details the kinetics of

electrochemical sodiation in the ball-milled BM-30 γ'-V_2O_5 as a function of depth of discharge and charge.

3.3. Kinetics study during the first discharge-charge process

AC impedance diagrams of discharged γ-$Na_xV_2O_5$ electrodes ($0 \leq x \leq 0.9$) are reported in **Fig. 6**. For $0.02 \leq x \leq 0.2$ (**Fig. 6a**), two components are observed at high frequency. In addition to the charge transfer semi-circle at 25 Hz, a second one appears at ≈ 1 Hz. This signal rapidly vanishes with sodiation and completely disappears for $x \geq 0.3$ (**Fig. 6a** and **6b**). Such a phenomenon was not observed in the case of as-synthesized γ'-V_2O_5 characterized by micrometric platelets and larger consistency domain of 90 nm [19]. This result is probably related to the smaller aggregates and crystallites size of the ball-milled sample (35 nm) for which an enhanced electrode reactivity toward electrolyte probably favours the formation of a passivating layer. The disappearance of the extra-semi-circle at ≈ 1 Hz from x = 0.3 suggests a consumption of this native layer through the increasing electrochemical process.

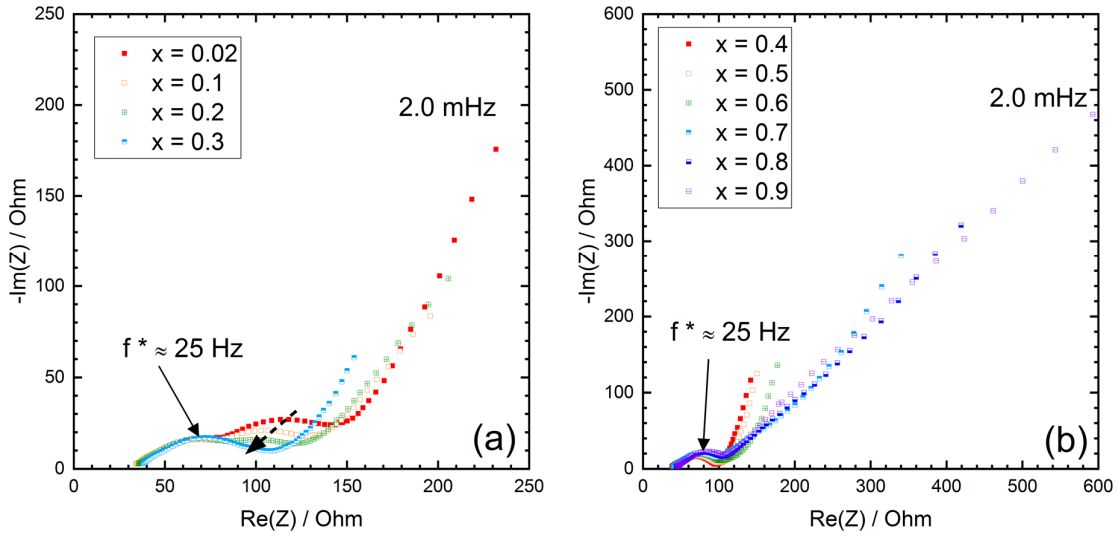

Figure 6. AC impedance diagrams of BM-30 γ-$Na_xV_2O_5$ during the first discharge in 1M $NaClO_4$ PC + FEC (2% vol.) electrolyte: (a) $0.02 \leq x \leq 0.3$; (b) $0.4 \leq x \leq 0.9$.

As shown in **Fig. S3** in SI, the Nyquist diagrams of the discharged BM-30 γ-$Na_xV_2O_5$ electrodes exhibit the conventional typical shape expected for an insertion compound [23]. The charge transfer semi-circle observed at 20-25 Hz is systematically followed by a straight-line with a phase angle of 45° from the real axis corresponding to the Warburg region relative to semi-infinite diffusion phenomenon ($\omega >> 2D_{Na}/L^2$; L being the maximum length of the diffusion pathway). Then, at lower frequencies, a capacitive line corresponding to finite diffusion is observed except for the most sodiated sample (x = 0.9) for which a slower diffusivity can be then expected.

The main kinetic parameters of the Na insertion reaction into BM-30 γ'-V_2O_5 like the cathode impedance $|Z|$ and the charge transfer resistance R_{ct} are reported in **Fig.S4** in SI as a function of the Na content x. The cathode impedance, in the range 200 Ω up to x = 0.6, suddenly increases by a factor 2 for x = 0.7 and 0.8 and once again by a factor 2 to reach 760 Ω for x = 0.9. In the same way, it is noteworthy the charge transfer resistance is quite constant up to the mid-discharge and then linearly increases upon further sodiation, from 62 Ω for x = 0.5 to 80 Ω for x = 0.9. A value of 0.3/0.4 mA cm^{-2} is found for the exchange current density j°, in line with usual j° values found for Li and Na insertion in transition metal oxides [16, 19, 23-26]. This slowdown in the charge transfer kinetics with sodiation can be understood if considering the highly localized character of electrons in the fully sodiated γ-$Na_{0.97}V_2O_5$ phase [27]. In addition, a partial loss of interparticle contact due to important volume change on sodiation (+18%, see **Fig. 4d**) cannot be discarded to explain the increase in the cathode impedance with sodiation.

The double layer capacity C_{dl} remains practically unchanged with values of ≈ 90 μF cm^{-2} all along the sodiation process. It is worth noting this mean value is 3 to 4 times higher than previously reported one for the as-synthesized γ'-V_2O_5 (20-30 μF cm^{-2}). This discrepancy reflects a higher electroactive surface area developed by the ball-milled BM-30 γ'-V_2O_5 (by a factor of 2-3) that

promotes a homogeneous sodiation reaction and a much improved rechargeability (90% at C/10 against only 50% for the as-synthesized oxide).

The systematic existence of a Warburg region in the impedance diagrams (**Fig. S3 in SI**) allows the apparent Na chemical diffusion coefficient D_{Na} to be calculated according to equation (1) [23].

$$A_w = V_M.(dE/dx)_x / F\sqrt{2}\, S\ D_{Na}^{1/2} \qquad \omega >> 2D_{Na}/L^2 \qquad \text{(eq. 1)}$$

A_w is the Warburg prefactor, V_M is the molar volume of the compound (V_M= 53.9 $cm^3.mol^{-1}$), S is the geometric surface area of the electrode (1cm^2), $(dE/dx)_x$ is the slope, at fixed x, of the equilibrium potential composition curve (**Fig. 2d**).

The analysis of the Warburg impedance of the system plotted in the complex plane Re(Z) vs $\omega^{-1/2}$ as a function of x in BM-30 γ-$Na_xV_2O_5$ electrodes allows to get the Warburg prefactor Aw (**Fig. 7a**). **Fig. 7b** displays the evolution of the apparent chemical diffusion coefficient of sodium ions $D_{Na,}$ as a function of x in BM-30 γ-$Na_xV_2O_5$ ($0 \leq x \leq 0.9$). A very high value ($\approx 10^{-8}$ cm^2 s^{-1}) is found for the very first inserted sodium ions (x= 0.02), then a lower and stable value around 10^{-10} cm^2 s^{-1} is observed during the first part of the discharge. In the second part of the discharge ($0.5 \leq x \leq 0.8$), a second set of values around 10^{-8}- 2 10^{-9} cm^2 s^{-1} is highlighted, reflecting a high sodium diffusivity in this region corresponding to a wide solid solution domain. For the fully discharged compound (x = 0.9), D_{Na} decreases due to the high sodium concentration but remains high, around 3.10^{-9} cm^2 s^{-1}. A straightforward comparison of the present data with the sodium diffusion rate previously reported for the as-synthesized γ'-V_2O_5 characterized by micrometric platelets [19] clearly indicates a better diffusion, at least by one order of magnitude whatever the sodium content. Such result can be ascribed to several positive issues provided by the ball-milling process: a decrease in the crystallite size by a factor 3, an increase in the electroactive surface area by a factor 2/3 favoring a more homogeneous sodiation-extraction process. Finally, the enhanced electrochemical performance of the ball-milled BM-30 material reveals a better accommodation of the structural stress afforded by

a peculiar Na reaction mechanism involving wide single-phase domains at the expense of the diphasic region.

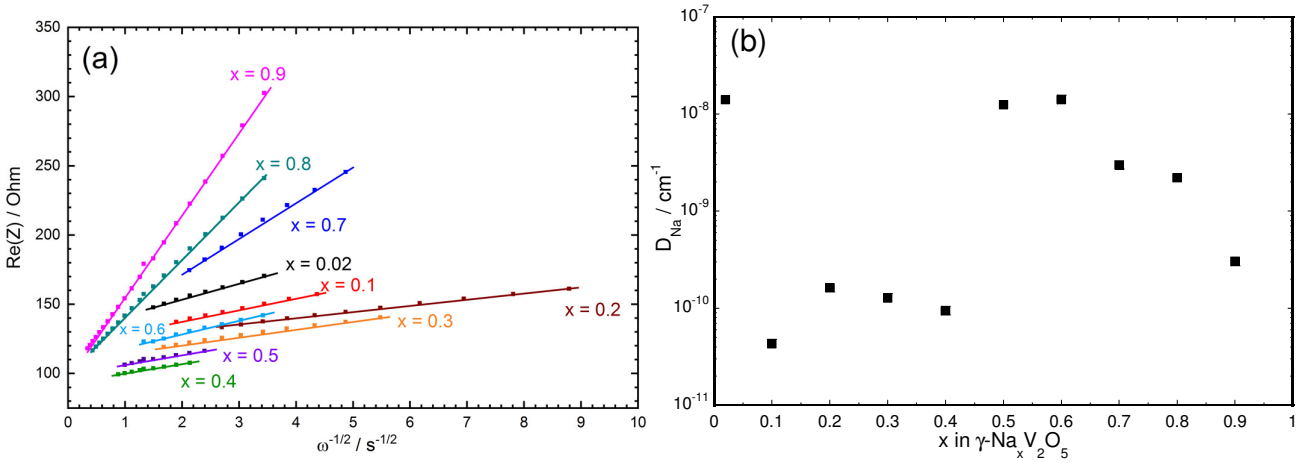

Figure 7. Compositional dependence of (a) the real part of the Warburg impedance Re(Z) vs $\omega^{-1/2}$; and (b) the apparent diffusion coefficient for Na ions D_{Na} during the first discharge of BM-30 γ-$Na_xV_2O_5$ in 1M $NaClO_4$ PC + FEC (2% vol.) electrolyte ($0 \leq x \leq 0.9$).

The Nyquist diagrams for the charged BM-30 γ-$Na_xV_2O_5$ electrodes are shown in **Fig. S5** in SI. All these impedance spectra, characterized by well-defined Warburg domain and the presence of a capacitive line at lower frequency, are practically superimposable to those recorded during the discharge (**Fig. 6**). This result points to similar kinetics for the Na insertion and extraction reactions in the ball-milled BM-30 γ'-V_2O_5 and accounts for the good charge efficiency achieved for this material. Such remarkable finding significantly differs from that revealed during the charge of the as-synthesized γ'-V_2O_5, characterized by a slower kinetics of charge transfer and much higher impedance values [19]. A comparison of the impedance spectra obtained for the same composition (x = 0.3 and x = 0.6) in discharge and charge (**Fig. 8**) confirms the good reversibility of the electrochemical reaction in BM-30 γ'-V_2O_5, these spectra showing very close profiles with similar impedance values and the systematic presence of a Warburg domain followed by a capacitive line.

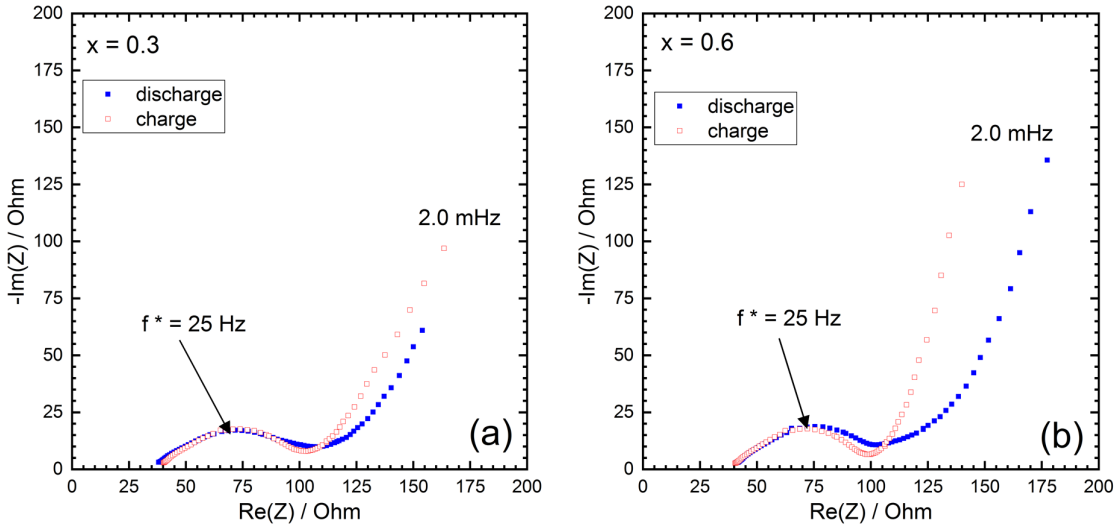

Figure 8. Comparison of AC impedance diagrams of discharged and charged BM-30 γ-$Na_xV_2O_5$ electrodes for the same x composition: (a) x = 0.3; (b) x = 0.6. Electrolyte 1M $NaClO_4$ PC + FEC (2% vol.).

4. Conclusion

In this work, we provided evidence for the enhanced electrochemical properties of γ'-V_2O_5 as sodium intercalation compound. An appropriate ball-milling procedure is shown to successfully solve the major drawback of γ'-V_2O_5 which consisted in a poor charge efficiency of the first cycle, limited to 50% at C/10 and much less at higher rates. The specific morphology of the ball-milled BM-30 γ'-V_2O_5 powder, made of small aggregates lower than 500 nm with mean crystallite size of 35 nm, promotes a uniform sodiation of γ'-V_2O_5 host lattice. As major consequence, the charge efficiency is greatly improved to around 90%, allowing excellent cycling properties to be achieved. The Na insertion mechanism in the ball-milled powder, investigated by XRD and Raman experiments, involves a peculiar structural answer of the γ-V_2O_5 framework: the particle size reducing by a factor 3 induces a noticeable shortening of the diphasic domain to the benefit of enlarged single-phase region ($0 \leq x < 0.2$ and $0.4 \leq x \leq 0.94$ in γ-$Na_xV_2O_5$). Such structural behaviour upon sodiation is in good agreement with the OCV and discharge-charge profiles showing wider sloping composition-voltage domain. The kinetic study by EIS reveals a significant increase in the electroactive surface area by a factor 2-3 allowing a fast and homogeneous sodiation of γ'-V_2O_5. Such finding accounts for the high rate capability exhibited by the ball-milled material, with 140 mAh g^{-1} recovered at C/10 and still 85 mAh g^{-1} at 2C. The linear increase in the Rct parameter from the mid-discharge reveals a decrease in the charge transfer kinetics due to the highly localized character of electrons in the γ-$Na_xV_2O_5$ phase. The composition dependence of the apparent chemical diffusion coefficient D_{Na} indicates an enhanced diffusion in the single-phase regions compared to the diphasic domain and a faster Na diffusivity, by one order of magnitude, in the ball-milled oxide than in the as-synthesized γ'-V_2O_5 powder. This work demonstrates the ball-milled BM-30 γ'-V_2O_5 is a high performance cathode material for SIBs due to its high working voltage of 3.2 V vs Na^+/Na similar to lithiation, its fast kinetics allowing high rate capability, excellent charge efficiency and good cycle life.

References

[1] N. Yabuuchi, K. Kubota, M. Dahbi, S. Komaba, Research developments on sodium-ion batteries, Chem. Rev. 114 (2014) 11636–11682. DOI: 10.1021/cr500192f

[2] L. Li, Y. Zheng, S. Zhang, J. Yang, Z. Shao, Z. Guo, Recent progress on sodium ion batteries: Potential high-performance anodes. Energy Environ. Sci. 11 (2018) 2310-2340. DOI: 10.1039/C8EE01023D

[3] R. Berthelot, D. Carlier, C. Delmas, Electrochemical Investigation of the P2–Na_xCoO_2 Phase Diagram, Nat. Mater. 10 (2011) 74-80. DOI: 10.1038/NMAT2920

[4] N. Yabuuchi, M. Kajiyama, J. Iwatate, H. Nishikawa, S. Hitomi, R. Okuyama, R. Usui, Y. Yamada, S. Komaba, V. P2-type $Na_x[Fe_{1/2}Mn_{1/2}]O_2$ made from earth-abundant elements for rechargeable Na batteries, Nat. Mater. 11 (2012) 512-517. DOI: 10.1038/nmat3309

[5] X. Ma, H. Chen, G. Ceder, G., Electrochemical properties of monoclinic $NaMnO_2$, J. Electrochem. Soc. 158 (2011) A1307-1312. DOI:10.1149/2.035112jes

[6] S. Komaba, C. Takei, T. Nakayama, A. Ogata, N. Yabuuchi, Electrochemical intercalation activity of layered $NaCrO_2$ vs. $LiCrO_2$, Electrochem. Commun. 12 (2010) 355-358. DOI: 10.1016/j.elecom.2009.12.033

[7] M. Guignard, C. Didier, J. Darriet, P. Bordet, E. Elkaim, C. Delmas, P2-Na_xVO_2 system as electrodes for batteries and electron-correlated materials, Nat. Mater. 12 (2013) 74-80. DOI: 10.1038/nmat3478

[8] D. Hamani, M. Ati, J. M.Tarascon, P. Rozier, Na_xVO_2 as possible electrode for Na-ion batteries, Electrochem. Comm. 13 (2011) 938-941. DOI: 10.1016/j.elecom.2011.06.005

[9] G. Venkatesh, V. Pralong, O. I. Lebedev, V. Caignaert, P. Bazin, B. Raveau, Amorphous sodium vanadate $Na_{1.5+y}VO_3$, a promising matrix for reversible sodium intercalation, Electrochem. Comm. 40 (2014) 100-102. DOI: 10.1016/j.elecom.2013.11.004

[10] S. Bach, N. Baffier, J. P. Pereira-Ramos, R. Messina, Electrochemical sodium intercalation in $Na_{0.33}V_2O_5$ bronze synthesized by a sol-gel process, Solid State Ion. 37 (1989) 41-49. DOI: 10.1016/0167-2738(89)90285-3

[11] H. M. Liu, H. S. Zhou, L. P. Chen, Z. F. Tang, W. S. Yang, Electrochemical insertion/deinsertion of sodium on NaV_6O_{15} nanorods as cathode material of rechargeable sodium-based batteries, J. Power Sources 196 (2011) 814-819. DOI: 10.1016/j.jpowsour.2010.07.062

[12] K. West, T. Zachau-Christiansen, T. Jacobsen, S. Skaarup, Sodium insertion in vanadium oxides, Solid State Ionics 28 (1988) 1128-1131. DOI: 10.1016/0167-2738(88)90343-8

[13] D. Muller, R. Baddour-Hadjean, M. Tanabe, L. T. N. Huynh, L. M. P. Le, J. P. Pereira-Ramos, Electrochemically formed α'-NaV_2O_5: a new sodium intercalation compound, Electrochim. Acta 176 (2015) 586-593. DOI: 10.1016/j.electacta.2015.07.030

[14] R. Baddour-Hadjean, L. T. N. Huynh, N. Emery, J. P. Pereira-Ramos, Lithium insertion in alpha'-NaV2O5: Na-pillaring effect on the structural and electrochemical properties, Electrochim. Acta, 270 (2018) 224-235. DOI: 10.1016/j.electacta.2018.03.087

[15] R. Baddour-Hadjean, M. Safrany Renard, J.P. Pereira-Ramos, Unraveling the strucrural mechanism of Li insertion in γ'-V_2O_5 and its effect on cycling properties, Acta Mater. 165 (2019) 183-191. DOI: 10.1016/j.actamat.2018.11.043.

[16] R. Baddour-Hadjean, M. Safrany Renard, J.P. Pereira-Ramos, Kinetic insight into the electrochemical lithium insertion process in the puckered-layer γ'-V_2O_5 polymorph. J. Electrochem. Soc., 166 (2019) A1-A6. DOI: 10.1016/j.electacta.2019.134670

[17] M. Safrany Renard, N. Emery, R. Baddour-Hadjean, J. P. Pereira-Ramos, γ'-V_2O_5: A new high voltage cathode material for sodium-ion battery, Electrochim. Acta 252 (2017) 4-11. DOI: 10.1016/j.electacta.2017.08.175

[18] R. Baddour-Hadjean, L.T. Huynh, N. Emery, J.P. Pereira-Ramos , The richness of V_2O_5 polymorphs as superior cathode materials for sodium insertion , Electrochim. Acta 270 (2018) 129-137. DOI: 10.1016/j.electacta.2018.03.062

[19] M. Safrany Renard, R. Baddour-Hadjean, J. P. Pereira-Ramos, Kinetic insight into the electrochemical sodium insertion-extraction mechanism of the puckered γ'-V_2O_5 polymorph, Electrochim. Acta 322 (2019) 134670. DOI: 10.1016/j.electacta.2019.134670

[20] M. Safrany Renard, N. Emery, E. M. Roginskii, R. Baddour-Hadjean, J. P. Pereira-Ramos, Crystal structure determination of a new sodium vanadium bronze electrochemically formed , J. Solid State Chem. 254 (2017) 62-68. DOI: 10.1016/j.jssc.2017.07.012

[21] J. Barker, M. Y. Saidi, J. L. Swoyer, Performance evaluation of the electroactive material γ-LiV_2O_5 made by a carbothermal reduction method, J. Electrochem. Soc. 150 (2003) A1267-A1272. DOI: 10.1149/1.1600462

[22] R. Baddour-Hadjean, M. B. Smirnov, V. Y. Kazimirov, K. S. Smirnov, J. P. Pereira-Ramos, The Raman spectrum of the γ′-V_2O_5 polymorph: a combined experimental and DFT study, J. Raman Spectrosc. 46 (2015) 406-412. DOI: 10.1002/jrs.4660

[23] C. Ho, I. D. Raistrick, R.A. Huggins, Application of AC techniques to the study of lithium diffusion in tungsten trioxide thin films, J. Electrochem. Soc., 127 (1980) 343-350. DOI: 10.1149/1.2129668

[24] J. Farcy, R. Messina, J. Perichon, Kinetic Study of the Lithium Electroinsertion in V_2O_5 by Impedance Spectroscopy, J. Electrochem. Soc., 137 (1990) 1337-1341. DOI: 10.1149/1.2086669

[25] D. Huo, B. Laïk, P. Bonnet, K. Guérin, R. Baddour-Hadjean, J. P. Pereira-Ramos, Electrochemical kinetics of Li insertion in nanosized high performance V_2O_5 obtained via fluorine chemistry, Electrochim. Acta 253 (2017) 472-478. DOI: 10.1016/j.electacta.2017.09.050

[26] B. Garcia, J. Farcy, J. P. Pereira-Ramos, N. Baffier, Electrochemical Properties of Low Temperature Crystallized $LiCoO_2$, J. Electrochem. Soc., 144 (1997) 1179-1184. DOI: 10.1149/1.1837569

[27] N. Emery, R. Baddour-Hadjean, D. Batyrbekuly, B. Laïk, Z. Bakenov, J-P. Pereira-Ramos, γ-$Na_{0.96}V_2O_5$: a new competitive cathode material for sodium ion battery synthesized by a soft chemistry route, Chem. Mater. 30 (2018) 5305−5314. DOI: 10.1021/acs.chemmater.8b02066

Figure captions

Figure 1. (A) SEM images and (B) XRD patterns of (a) as-synthesized (b) BM-30 (c) BM-40 (d) BM-60 γ'-V_2O_5. Red stars in Figure 1B: reflections of α-V_2O_5. Inset in Figure 1A: Crystalline structure of γ'-V_2O_5.

Figure 2. (a) First discharge-charge cycle at C/10 rate of as-synthesized and BM-30 γ'-V_2O_5 (b) Cycling curves of BM-30 γ'-V_2O_5 at C/2 rate (c) Evolution of the specific discharge capacity during cycling at different C-rates of as-synthesized γ'-V_2O_5 (black symbols △▲) and BM-30 γ'-V_2O_5 (red symbols □■) (d) OCV discharge curve of BM-30 γ'-V_2O_5 Electrolyte 1M $NaClO_4$ PC + FEC (2% vol.).

Figure 3. XRD patterns of BM-30 γ-$Na_xV_2O_5$ during the first discharge-charge cycle in 1M $NaClO_4$ PC + FEC (2% vol.) electrolyte; (a) discharge ($0 \leq x \leq 0.94$); (b) charge ($0.1 \leq x \leq 0.94$). ● Graphite peaks. ■ Stainless steel grid.

Figure 4. Evolution of (a-b-c) the unit cell parameters and (d) volume of the phases formed during the first discharge-charge cycle of BM-30 γ'-V_2O_5 in 1M $NaClO_4$ PC + FEC (2% vol.) : ■ discharge ⌗ charge ($0 \leq x \leq 0.94$).

Figure 5. Raman spectra of BM-30 γ-$Na_xV_2O_5$ during the first discharge-charge cycle in 1M $NaClO_4$ PC + FEC (2% vol.) electrolyte: (a) discharge ($0 \leq x \leq 0.94$); (b) charge ($0.1 \leq x \leq 0.94$).

Figure 6. AC impedance diagrams of BM-30 γ-$Na_xV_2O_5$ during the first discharge in 1M $NaClO_4$ PC + FEC (2% vol.) electrolyte: (a) $0.02 \leq x \leq 0.3$; (b) $0.4 \leq x \leq 0.9$.

Figure 7. Compositional dependence of (a) the real part of the Warburg impedance Re(Z) vs $\omega^{-1/2}$; and (b) the apparent diffusion coefficient for Na ions D_{Na} during the first discharge of BM-30 γ-$Na_xV_2O_5$ in 1M $NaClO_4$ PC + FEC (2% vol.) electrolyte ($0 \leq x \leq 0.9$).

Figure 8. Comparison of AC impedance diagrams of discharged and charged BM-30 γ-$Na_xV_2O_5$ electrodes for the same x composition: (a) x = 0.3; (b) x = 0.6. Electrolyte 1M $NaClO_4$ PC + FEC (2% vol.).

Highlights

- Enhanced performance of ball-milled γ'-V_2O_5 as cathode material for SIB.
- Positive impact of particle size reduction on rechargeability and cycle life.
- Peculiar Na insertion mechanism showing wide solid solution domains.
- Enhanced Na diffusion in the single-phase regions vs. diphasic one.
- Faster Na diffusivity in the ball-milled vs. as-synthesized γ'-V_2O_5

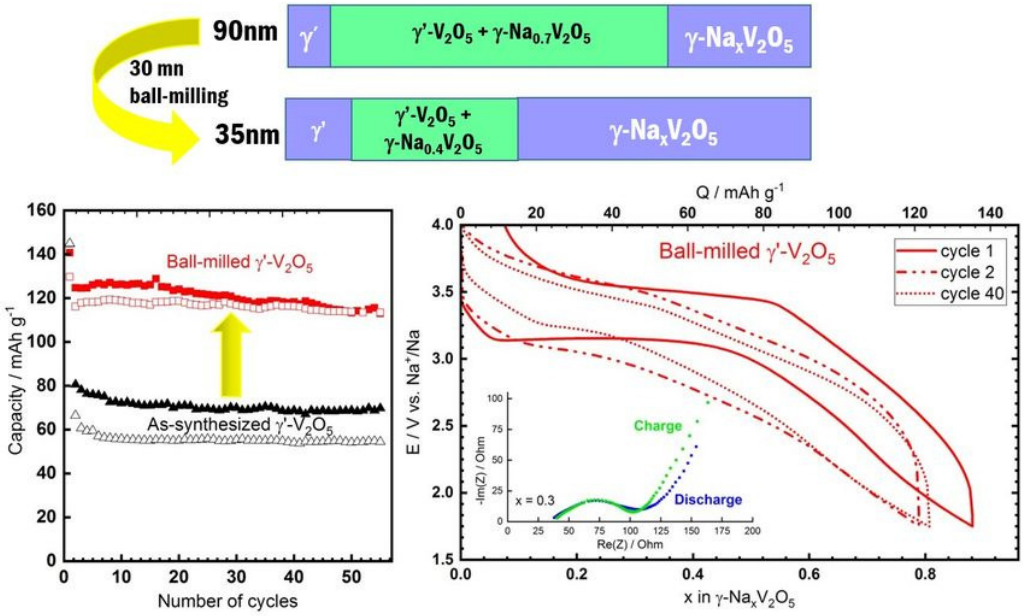
90nm
30 mn
ball-milling
35nm
γ´
γ'-V2O5 + γ-Na0.7V2O5
γ-NaxV2O5
γ'
γ'-V2O5 +
γ-Na0.4V2O5
γ-NaxV2O5
Capacity / mAh g-1
Number of cycles
Ball-milled γ'-V2O5
As-synthesized γ'-V2O5
Q / mAh g-1
E / V vs. Na+/Na
x in γ-NaxV2O5
Ball-milled γ'-V2O5
cycle 1
cycle 2
cycle 40
Charge
Discharge
x = 0.3
-Im(Z) / Ohm
Re(Z) / Ohm

Enhanced Electrochemical Properties of Ball-Milled γ'-V_2O_5 as Cathode Material for Na-ion Batteries: A Structural and Kinetic Investigation

Rita Baddour-Hadjean*, Marianne Safrany Renard, Jean-Pierre Pereira-Ramos[+]

Institut de Chimie et des Matériaux Paris Est (ICMPE), UMR 7182 CNRS-Université Paris Est Créteil, 2 rue Henri Dunant, 94320 Thiais, France

*corresponding author: baddour@icmpe.cnrs.fr, ORCID ID 0000-0002-3158-1851
[+]ORCID ID 0000-0001-5381-900X

Supplementary Information

Figure S1. Raman spectra of (a) as-synthesized γ'-V_2O_5 (b) BM-30 γ'-V_2O_5 (c) BM-40 γ'-V_2O_5 (d) BM-60 γ'-V_2O_5. Red stars: Raman lines of α-V_2O_5.

Figure S2. Influence of the C rate (C/20-2C range) on the charge capacity recovered during the first cycle of γ'-V_2O_5 as-synthesized (dark blue) and ball-milled during 30 mn (light blue). Electrolyte 1M $NaClO_4$ PC + FEC (2% vol.).

Figure S3. Nyquist diagrams of selected discharged BM-30 γ-$Na_xV_2O_5$ electrodes: (a) x = 0.02; (b) x = 0.3; (c) x = 0.6; (d) x = 0.9. Electrolyte 1M $NaClO_4$ PC + FEC (2% vol.).

Figure S4. Evolution of (a) the cathode impedance ($|Z|$) and (b) charge transfer resistance (R_{ct}) of BM-30 γ-$Na_xV_2O_5$ during the first discharge in 1M $NaClO_4$ PC + FEC (2% vol.) electrolyte ($0 \leq x \leq 0.9$).

Figure S5. AC impedance diagrams of BM-30 γ-$Na_xV_2O_5$ during the first charge in 1M $NaClO_4$ PC + FEC (2% vol.) electrolyte: (a) $0.1 \leq x \leq 0.5$; (b) $0.6 \leq x \leq 0.8$

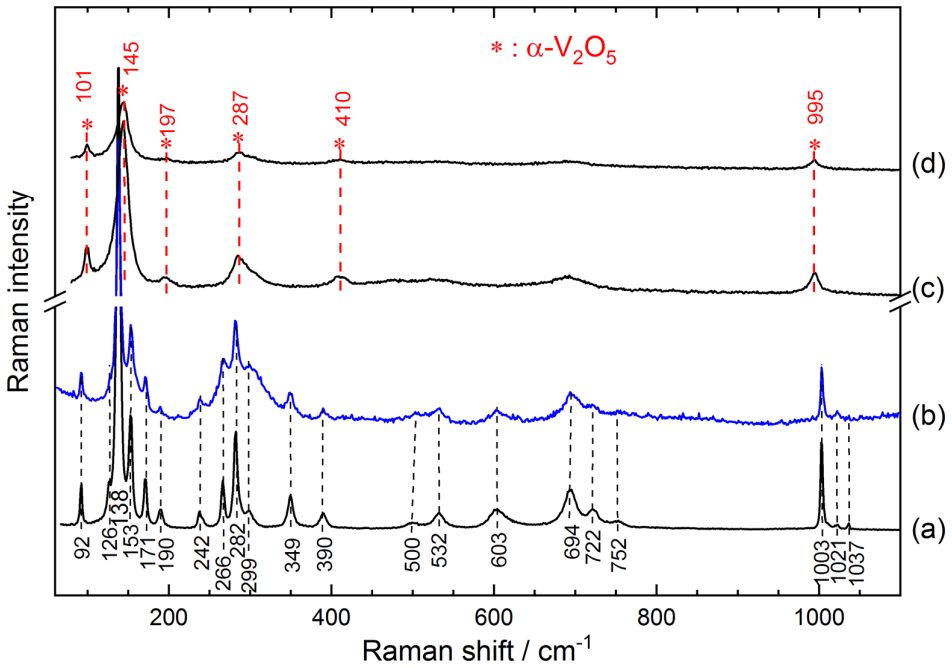

Figure S1. Raman spectra of (a) as-synthesized γ'-V_2O_5 (b) BM-30 γ'-V_2O_5 (c) BM-40 γ'-V_2O_5 (d) BM-60 γ'-V_2O_5. Red stars: Raman lines of α-V_2O_5.

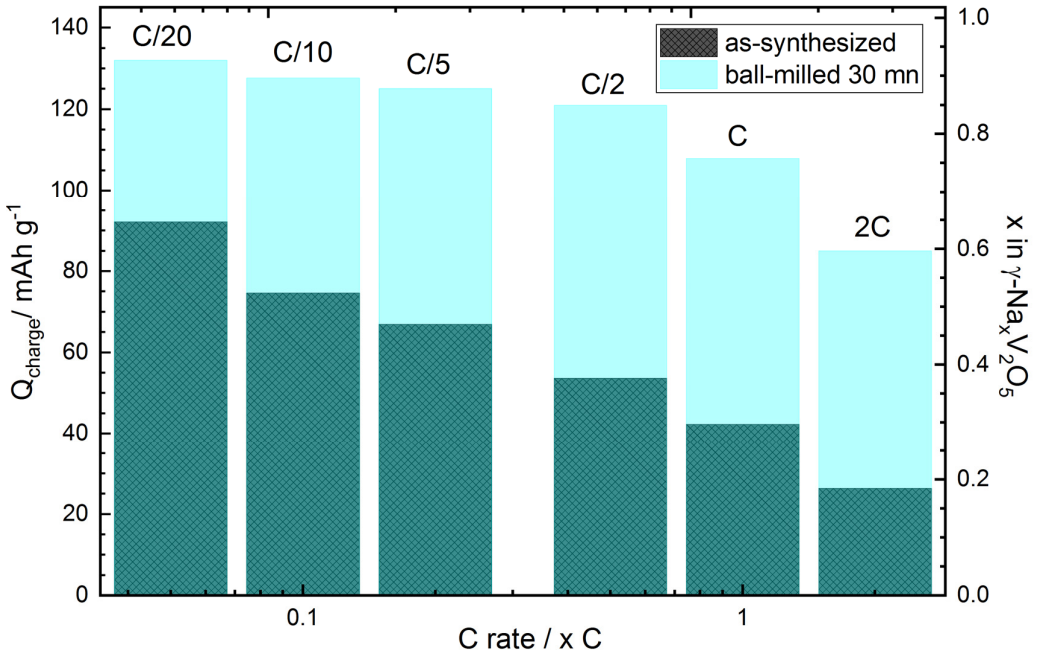

Figure S2. Influence of the C rate (C/20-2C range) on the charge capacity recovered during the first cycle of γ'-V_2O_5 as-synthesized (dark blue) and ball-milled during 30 mn (light blue). Electrolyte 1M $NaClO_4$ PC + FEC (2% vol.).

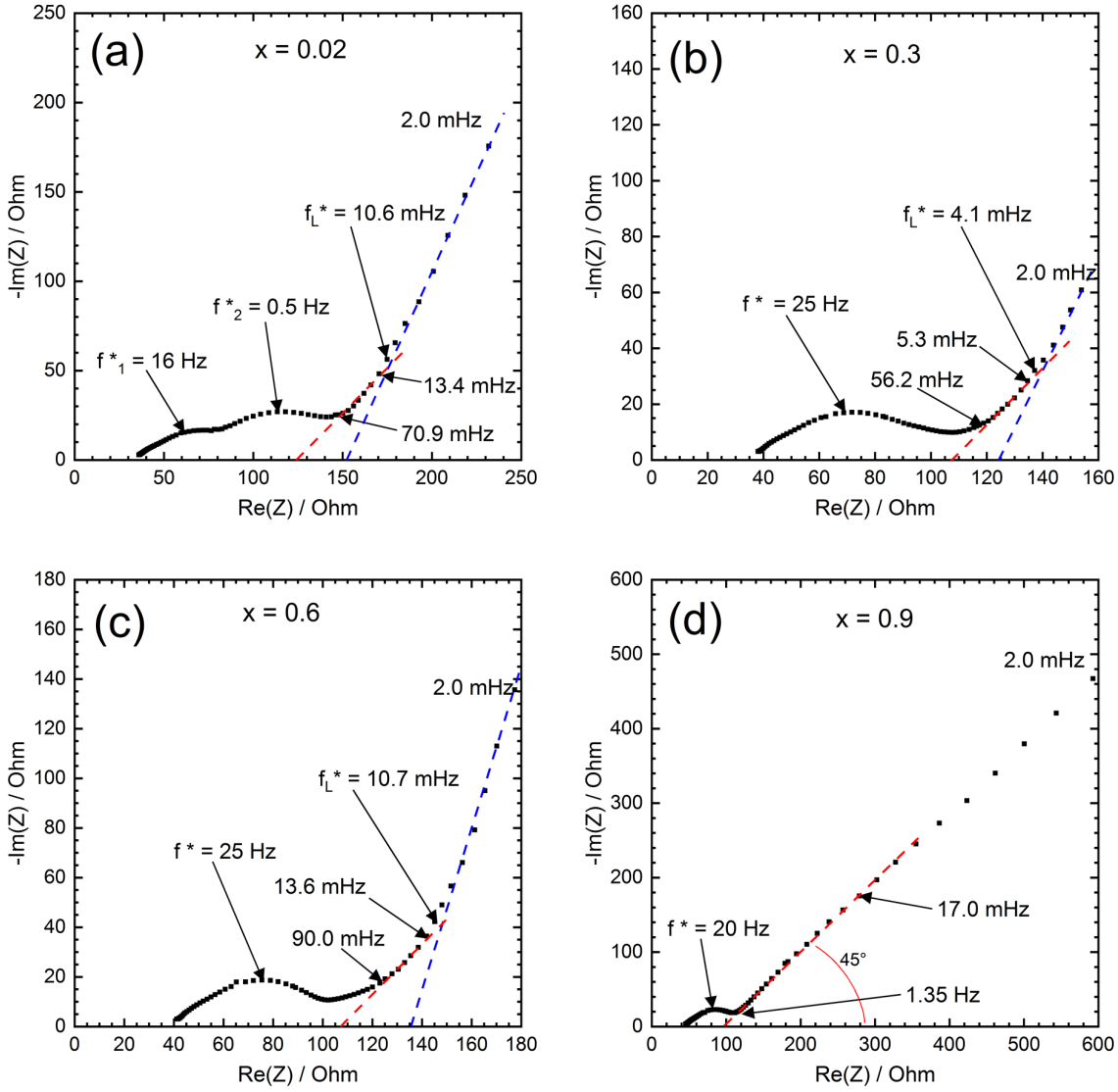

Figure S3. Nyquist diagrams of selected discharged BM-30 γ-$Na_xV_2O_5$ electrodes: (a) x = 0.02; (b) x = 0.3; (c) x = 0.6; (d) x = 0.9. Electrolyte 1M $NaClO_4$ PC + FEC (2% vol.).

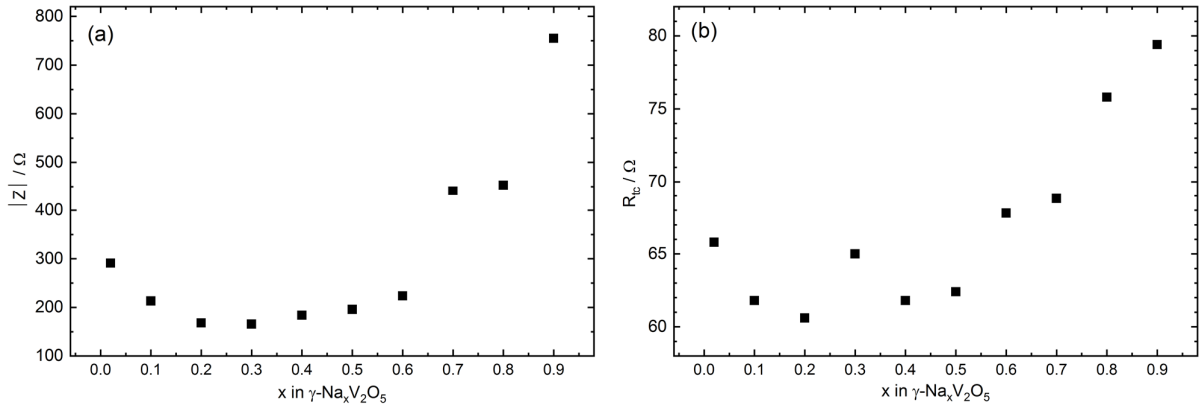

Figure S4. Evolution of (a) the cathode impedance ($|Z|$) and (b) charge transfer resistance (R_{ct}) of BM-30 γ-$Na_xV_2O_5$ during the first discharge in 1M $NaClO_4$ PC + FEC (2% vol.) electrolyte ($0 \leq x \leq 0.9$).

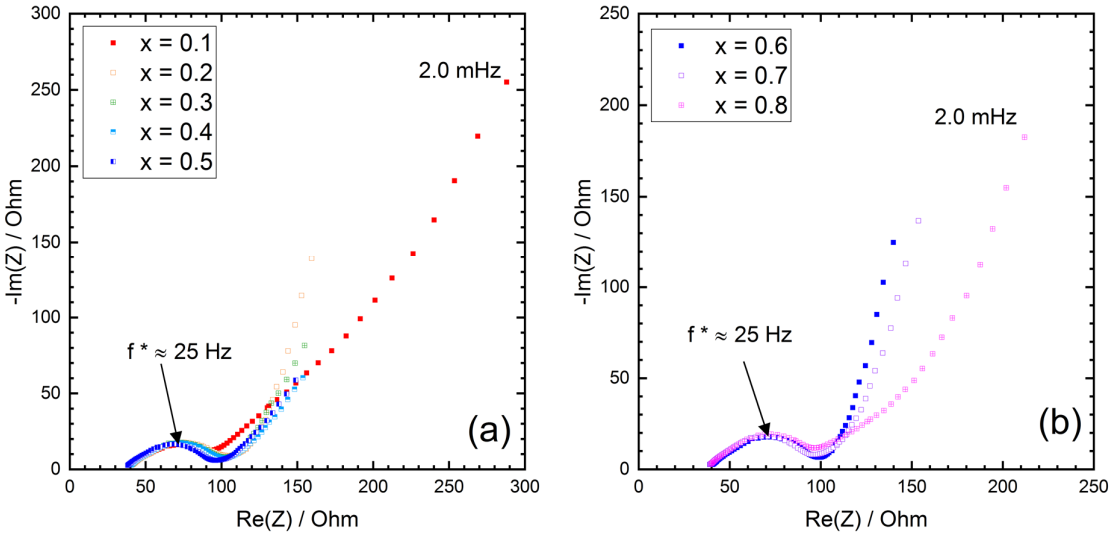

Figure S5. AC impedance diagrams of BM-30 γ-$Na_xV_2O_5$ during the first charge in 1M $NaClO_4$ PC + FEC (2% vol.) electrolyte: (a) $0.1 \leq x \leq 0.5$; (b) $0.6 \leq x \leq 0.8$